PAPER

Check for updates

Continuous flow extraction of lithium from brine using silica-coated LMO beads

Jialun Su,†[a] Qiyue Fan,†[a] Xiangting Hu,[a] Yue Sun,[a] Jie Lin,[a] Jiayue Xu,[a] Bingcai Pan [ID][bc] and Zhenda Lu [ID]*[ac]

The increasing demand for lithium-ion batteries in the electric vehicle market has intensified the demand for efficient lithium extraction from salt lake brine. This study presents a novel approach using silica-coated lithium manganese oxide (LMO) adsorbents embedded in millimeter-sized sodium alginate (SA) beads (LMO@SiO$_2$/SA beads). By replacing expensive and environmentally detrimental tetraethyl orthosilicate (TEOS) with low-cost, eco-friendly sodium metasilicate (Na$_2$SiO$_3$), we have developed a more sustainable and cost-effective lithium extraction method. Continuous flow adsorption–desorption experiments demonstrated the excellent performance of the LMO@SiO$_2$/SA beads, maintaining a lithium adsorption capacity of 6.22 mg g^{-1} and a consistent manganese dissolution ratio of 1.26% per cycle after 50 cycles. These results highlight the potential of this approach for large-scale lithium extraction from salt lakes, providing a sustainable and economical option to support the growing electric vehicle industry.

Introduction

The global increase in electric vehicles has intensified the demand for lithium, a critical component in lithium-ion batteries.[1–7] While traditional ore extraction methods face limitations in meeting this growing demand, salt lakes offer a more abundant and environmentally friendly source of lithium.[8–15] However, extracting lithium from salt lake brine presents challenges due to the low concentration and high magnesium-to-lithium ratio.[16–19]

Various methods have been proposed for lithium extraction, including lime soda evaporation,[20] electrochemical recovery,[21–27] and selective adsorption.[28–36] Among these methods, selective adsorption offers several advantages, such as simplicity, low cost, and fast kinetics. While previous studies have explored lithium manganese oxide (LMO) adsorbents, their susceptibility to acid dissolution during desorption limits their practical applications.

To address this issue, we introduce a novel approach using silica-coated LMO adsorbents embedded in millimeter sized sodium alginate beads (LMO@SiO$_2$/SA). In this method, sodium metasilicate (Na$_2$SiO$_3$) was applied as a more

sustainable and cost-effective silicon source compared to traditional TEOS coating methods. Additionally, sodium alginate is employed to make millimeter-sized composite beads, enabling continuous flow extraction, a crucial aspect for industrial applications. Our results demonstrate excellent lithium adsorption performance, with an adsorption capacity of 6.22 mg g^{-1} and a minimal manganese dissolution ratio of 1.26% per cycle after 50 cycles. These findings highlight the potential of our approach to meet the growing demand for lithium while addressing the challenges associated with traditional extraction methods.

Materials and methods

Experimental materials

Lithium manganese oxide (LMO, Taiyuan Lizhiyuan Technology Co., Ltd), deionized water (DIW), hydrochloric acid (HCl, Sinopharm Chemical Reagent Co., Ltd), ethanol (Sinopharm Chemical Reagent Co., Ltd), polyacrylic acid (PAA, Macklin Biochemical Co., Ltd), sodium metasilicate nonahydrate (Na$_2$SiO$_3$·9H$_2$O, AR, Sinopharm Chemical Reagent Co., Ltd), DT-135 defoamer (Xushi Chemical Technology Co., Ltd), sodium alginate ((C$_6$H$_7$O$_6$Na)$_n$, Aladdin Biochemical Technology Co., Ltd), anhydrous calcium chloride (CaCl$_2$, Macklin Biochemical Co., Ltd), magnesium chloride hexahydrate (MgCl$_2$·6H$_2$O, AR, Aladdin Biochemical Technology Co., Ltd), lithium chloride (LiCl, Aladdin Biochemical Technology Co., Ltd), potassium chloride (KCl, 99.5%, Macklin Biochemical Co., Ltd), and analytical grade sodium chloride (AR, Sinopharm Chemical Reagent Co., Ltd) were used.

[a] College of Engineering and Applied Sciences, State Key Laboratory of Analytical Chemistry for Life Science, and Jiangsu Key Laboratory of Artificial Functional Materials, Nanjing University, Nanjing 210093, China. E-mail: luzhenda@nju.edu.cn

[b] State Key Laboratory of Pollution Control and Resource Reuse, School of the Environment, Nanjing University, Nanjing 210023, China

[c] Research Center for Environmental Nanotechnology (ReCENT), Nanjing University, Nanjing 210023, China

† J. Su and Q. Fan contributed equally to this work.

Synthesis of LMO@SiO$_2$/SA beads

LMO pretreatment. The pretreatment step involves ball-milling and sieving of lithium manganese oxide (LMO). A pre-designed amount of LMO is placed into a ball mill and milled for ten cycles under the condition of a speed of 2000 rpm and each cycle lasting 5 minutes. This process reduces the particle size of LMO from 20–50 μm to approximately 0.5–5 μm. After ball-milling, the milled sample is transferred into 2 L of ethanol, stirred, and subjected to ultrasonication. Concurrently, the supernatant is extracted by centrifugation. After this, the sample is dried in an oven at 60 °C for 24 h and then stored in glass bottles for further use or analysis. This method ensures the preparation of finely milled LMO.

Synthesis of LMO@SiO$_2$

12 g of pretreated LMO was added into 200 mL of deionized water and the mixture was stirred for 1 hour and ultrasonically treated for 15 minutes to ensure good dispersion of lithium manganese oxide (LMO). 1.2 g of polyacrylic acid (PAA) was added into above mixture solution and continued stirring for an additional 8 hours. Subsequently, 30 g of nonahydrate sodium silicate were added into a 150 mL glass beaker, which was then set in a water bath and heated for 30 minutes until the sodium silicate was completely dissolved. This solution was poured into the pre-treated LMO solution and stirred for another 24 hours. After this, the mixture was transferred to a vacuum oven and dried at 240 °C to remove excess water. Eight drops of an antifoaming agent was added and then the dry mixture was transferred to a crucible and calcined at 500 °C for 4 hours in a muffle furnace. The crucible was removed, and the solidified mass was ground using a mortar to produce a fine LMO@SiO$_2$ powder.

Synthesis of HMO@SiO$_2$

0.1 g of LMO@SiO$_2$ was weighed and added into a 250 mL beaker. The mixture was washed with 200 mL of hydrochloric acid at a pH of 1 for one hour. After acid washing, the mixture was centrifuged and oven dried, and the sample HMO@SiO$_2$ powder was obtained.

Synthesis of LMO@SiO$_2$/SA beads

40 g of LMO@SiO$_2$ was weighed and added into a 1 L beaker. 700 mL of deionized water was added and stirred for 30 minutes followed by ultrasonication for 10 minutes. Then, 20 g of sodium alginate (SA) was added into the beaker and stirring was continued. The resulting LMO/SA solution was stored in a refrigerator to prevent aggregation of large molecular chains. The LMO/SA solution was loaded into a 50 mL syringe, the infusion pump was set at a rate of 1.5 mL min^{-1} with a total volume of 50 mL per injection, and a mixed solution of calcium chloride and PAA was used as a coagulation bath for granulation.

Continuous flow adsorption–desorption cycle experiments

Construction of a continuous flow adsorption–desorption system. Two adsorption columns with an inner diameter of 44 mm, an outer diameter of 50 mm, and an effective adsorption length of 300 mm were prepared. A peristaltic pump was acquired with dual channels and a maximum flow rate of 1140 mL min^{-1}. The peristaltic pump, adsorption columns, and high borosilicate glass containers were connected in series using silicone tubing with the following specifications: an inner diameter of 2.4 mm, an outer diameter of 5.6 mm, and a wall thickness of 1.6 mm. The system was secured within a fume hood, and the columns were filled with granulated LMO@SiO$_2$/SA beads to establish a continuous flow adsorption–desorption system.[1,16,17,37,38]

Preparation of simulated brine and extraction solution

To prepare models or simulated salt lake water, 57.75 g of anhydrous calcium chloride, 352.5 g of hexahydrate magnesium chloride, 4.585 g of lithium chloride, 52.2 g of potassium chloride, and 69.57 g of sodium chloride were added into a 2-liter bottle. The bottled was filled to the mark with deionized water to prepare a solution with a lithium chloride content of 1000 ppm. 444.44 mL of this solution was taken and transferred to a 5-liter plastic container and then 4 L of deionized water and 3 drops of 12 M hydrochloric acid were added to adjust the pH to 6.8, resulting in simulated salt lake water with a lithium chloride content of 100 ppm.

For the acidic lithium extraction solution, 4 L of deionized water was taken in a 5-liter plastic cylinder and 50 mL of 12 M hydrochloric acid was added to achieve a solution with a pH of 1 for acid extraction.

Continuous flow extraction cycle

The extraction system of the continuous flow operates in two main stages:

(i) Acid-washing stage: after filling the column with LMO@SiO$_2$/SA beads, 800 mL of pH = 1 HCl solution was used for lithium desorption, and the material was transformed into HMO@SiO$_2$/SA beads. The concentrations of Li$^+$ and Mn^{2+} were then measured using ICP-OES to calculate the desorption ratio of Li$^+$ and the leakage ratio of Mn^{2+}. The formulas are as follows:[16]

$$\text{Li}^+ \text{ desorption ratio} = \frac{C_{e1} \times V}{m} \times 100\%$$

$$\text{Mn}^{2+} \text{ desorption ratio} = \frac{C_{e2} \times V}{m} \times 100\%$$

where C_{e1} and C_{e2} are the concentrations of desorbed Li$^+$ and Mn^{2+}, respectively, V is the volume of the acidic lithium-extracting solution, and m is the mass of the adsorbent.

(ii) Adsorption stage: 800 mL of simulated salt lake water was pumped into the column containing HMO@SiO$_2$/SA beads for the adsorption experiment, after which the material was converted to LMO@SiO$_2$/SA beads. The concentration of Li$^+$ was determined using ICP-OES to calculate the Li$^+$ adsorption capacity using the formula:

$$q_e = \frac{(C_0 - C_e) \times V}{m}$$

where C_0 is the initial concentration of Li$^+$, Ce is the measured concentration of Li$^+$ post-adsorption, V is the volume of the

simulated salt lake water, and m represents the mass of the adsorbent. This stage evaluates the efficacy of the beads in capturing lithium from the solution and assesses the stability of the adsorbent over repeated cycles.

Characterization techniques

The surface morphology of samples was revealed by SEM (SEM, Ultra 55, Zeiss, Germany). TEM characterization was used to demonstrate the crystal structure, and the element analysis of nanoparticles was obtained using an FEI Tecnai F20 microscope equipped with an energy-dispersive spectroscopy detector operating at 200 kV (TEM, Tecnai G2 F20 X-TWIN, FEI, USA). The concentration of the Li^+ and Mn^{2+} in the solution was determined using an inductively coupled plasma optical-emission spectrometer (ICP-OES, iCAP 7400, Thermo Scientific, USA). Nitrogen adsorption measurements at 77 K were performed to study the porosity and specific surface area of the material (Brunauer–Emmett–Teller, Micromeritics TriStar 3000, USA). XRD (X-ray diffraction) patterns were used to analyze the phase change and crystalline structures of samples using an X-ray diffractometer (Ultima III, Rigaku, Japan).

Results and discussion

Fig. 1a schematically illustrates the preparation process of LMO@SiO$_2$. As shown in Fig. 1b, X-ray diffraction (XRD) analysis was conducted on both the ball-milled LMO powder and the calcined LMO@SiO$_2$ powder. The diffraction peaks of the LMO@SiO$_2$ powder at 18.76°, 36.34°, and 44.18° closely align with those of the ball-milled LMO powder, corresponding to the spinel (111), (311), and (400) planes, respectively.[39–41] These planes are formed by lithium in the tetrahedral sites and manganese in the octahedral centers.[42,43] The XRD results confirm that our LMO powder is composed of spinel-structured LiMn$_2$O$_4$, a key characteristic of lithium ion sieves. This structure enables the lithium ion sieve (LIS) to maintain vacancies left after lithium extraction in acidic solutions, thereby selectively adsorbing lithium ions.[44]

As depicted in Fig. 1c–f, we examined uncoated LMO and calcined LMO@SiO$_2$ powders using scanning electron microscopy (SEM). The SEM images reveal that the surface of uncoated LMO is relatively smooth. After coating and calcination with sodium silicate, a uniform silicon dioxide (SiO$_2$) layer is observed to encapsulate the LMO surface at both the 5 μm and 500 nm scales, indicating effective encapsulation by sodium silicate calcination.

To further analyze the SiO$_2$ layer formed after sodium silicate calcination, transmission electron microscopy (TEM) was employed to study the encapsulation of LMO@SiO$_2$, as shown in Fig. 1g–j. Fig. 1g demonstrates a well-defined silicon dioxide coating with distinct contrasts. *In situ* energy-dispersive X-ray spectroscopy (EDS) analysis in Fig. 1h–i clearly reveals that the Si signal map overlaps with the Mn signal map, indicating a uniform element distribution. Additionally, line-scan TEM analysis performed across the dashed line in Fig. 1j,

and as illustrated in Fig. 1k, further confirms that the silicon dioxide layer primarily encases the LMO after sodium silicate calcination. This encapsulation is expected to significantly reduce manganese dissolution in acidic solutions.

Severe manganese dissolution occurs during lithium elution in acidic solutions, leading to the destruction of the lithium ion sieve framework and poor adsorption–desorption cycle performance.[31,45] This hinders the industrial application of lithium ion sieves. Fig. 2a illustrates the manganese dissolution process. During acid washing, the delithiation of LMO is accompanied by the disproportionation reaction of Mn^{3+}, where Mn^{3+} transforms into Mn^{2+} and Mn^{4+} in acidic solutions. Mn^{2+} tends to dissolve in the solution, disrupting the LMO spinel structure, as shown in the following reaction:[46,47]

$$4Li[Mn^{3+}Mn^{4+}]O_4 + 8H^+ \rightarrow 3[Mn_2{}^{4+}]O_4 + 4Li^+ + 2Mn^{2+} + 4H_2O$$

In this study, we coated LMO with sodium silicate and obtained coated LMO@SiO$_2$ after calcination. This significantly reduces the ratio of manganese dissolution in acidic solutions and greatly enhances the cycle life due to the excellent protective properties of the SiO$_2$ coating layer. Compared with the typical silicon coating source TEOS, the affordability and availability of sodium silicate enable great potential for industrial applications. Fig. 2b describes the adsorption–desorption process of the LMO@SiO$_2$ adsorbent. The LMO@SiO$_2$ powder transforms into HMO@SiO$_2$ (HMO, the Li^+ sites in LMO were occupied by H^+) in the acidic solution. After centrifugation and drying, the HMO@SiO$_2$ powder is collected and used in the subsequent lithium adsorption process. The acidic solution contains certain amounts of Mn^{2+} and Li^+. Further centrifugation, titration, and ICP-OES analysis allow us to calculate the dissolution ratio of Mn^{2+} and the desorption ratio of Li^+.

Control experiments were conducted with uncoated LMO and coated LMO@SiO$_2$ powders in acidic solutions of different pH values. As shown in Fig. 2c, under various acidic conditions, the coated LMO@SiO$_2$ material exhibits a lower manganese dissolution ratio and a higher lithium desorption ratio. In the acid washing process to recover lithium, the SiO$_2$ coating reduced the manganese ion dissolution ratio from 10.93% to 2.82% at pH = 1, a decrease of approximately 74%. However, the SiO$_2$ coating slightly impacted the lithium ion desorption ratio. At pH = 0.5 and pH = 1, the uncoated lithium ion desorption ratios were 99.67% and 91.35%, respectively, while after coating, these ratios dropped to 75.70% and 70.82%. At pH = 2, both the manganese ion dissolution and lithium ion desorption ratios for coated and uncoated LMO materials were below 3% and 20%, respectively, indicating that lithium ions could not be effectively extracted from the LMO material at this pH level. These results suggest that the SiO$_2$ coating is an effective way to improve the selectivity of lithium ion recovery from spent lithium-ion batteries. In acid washing environments with pH = 0.5 and pH = 1, the manganese ion dissolution ratio significantly decreased after the SiO$_2$ layer coating, with the most notable reduction observed at pH = 1, where the ratio dropped from 10.93% to 2.82%, a decrease of approximately 74%. However, the SiO$_2$ coating
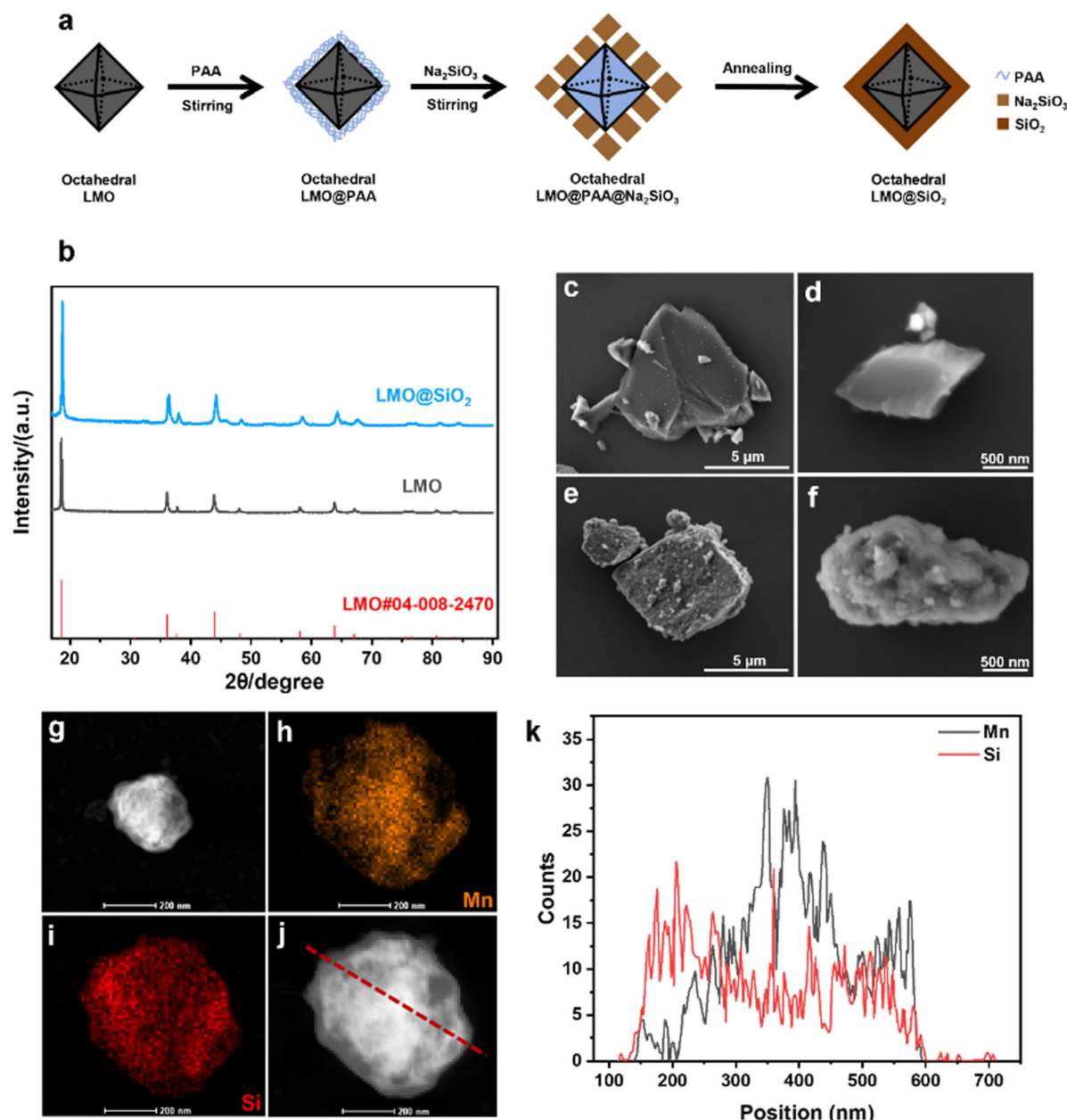
Fig. 1 (a) Schematic illustration of the preparation process of LMO@SiO$_2$. (b) XRD patterns of LMO before and after coating (LMO/LMO@SiO$_2$). (c)–(f) SEM images of LMO at various sizes before and after coating (LMO/LMO@SiO$_2$). (g) TEM images of LMO@SiO$_2$. (h)–(i) The EDS characterization of Mn and Si elements in the TEM image (g). (j)–(k) *In situ* TEM line scan of Mn and Si signals in LMO@SiO$_2$, and the corresponding element distribution along the red line from left to right.

slightly impacted the lithium ion desorption ratio. At pH = 0.5 and pH = 1, the uncoated lithium ion desorption ratios were 99.67% and 91.35%, respectively, while after coating, these ratios dropped to 75.70% and 70.82%. At pH = 2, although the manganese ion dissolution ratio for coated and uncoated LMO materials were below 3%, both the lithium ion desorption ratios were below 20%, indicating that lithium ions could not be effectively extracted from the LMO material at this pH level. Therefore, at low pH values (0.5 and 1), the SiO$_2$ layer effectively prevents the leakage of manganese ions from the LMO spinel structure, thereby maintaining the integrity of the LMO structure

and enhancing its adsorption–desorption cycle performance. Although the lithium desorption ratio is lower than that of the uncoated material due to the silica layer also affecting the free movement of Li$^+$, this is considered acceptable. Specifically, while the silica coating moderately decreased lithium desorption efficiency (by ∼20% at pH 0.5 and 1), it significantly enhanced adsorbent stability, reducing the manganese dissolution ratio by over 70%.

In industrial applications, the operation of powdered lithium extraction materials can be challenging due to significant losses during adsorption and desorption. These materials
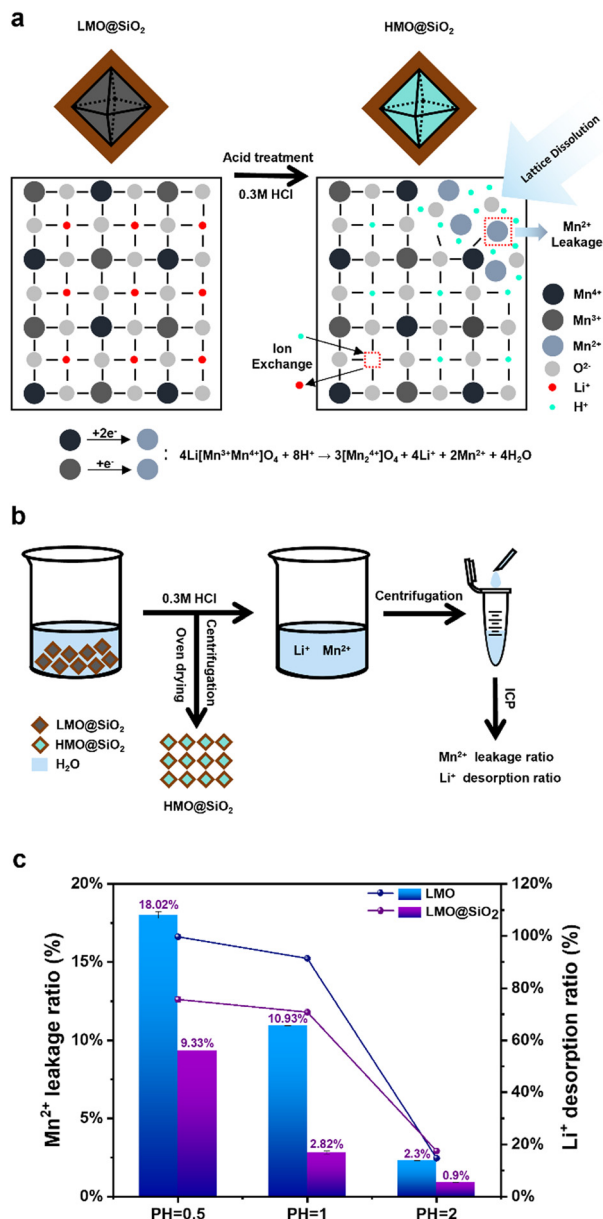
Fig. 2 (a) Schematic representation of the mechanism and dissolution process from LMO@SiO$_2$ to HMO@SiO$_2$ acid treatment. (b) Schematic diagram of Li$^+$ and Mn^{2+} adsorption–desorption processes and ICP characterization of treated solutions. (c) Li$^+$ desorption and Mn^{2+} leakage ratio of LMO and LMO@SiO$_2$ at different pH values.

often wash out with the flow of brine, leading to issues such as system blockages, poor fluidity, and low material recovery rates.[17] To address these problems, it is important to process the materials into granules. This paper utilizes environmentally friendly and renewable sodium alginate to granulate LMO@-SiO$_2$ using a sol–gel templating method, as illustrated in Fig. 3a. Sodium alginate rapidly forms a gel under mild conditions. When divalent cations like Ca^{2+} are present, an ion exchange reaction occurs between the Na$^+$ on the G units and the divalent cations, leading to the accumulation of G units and the formation of a cross-linked network structure, resulting in a hydrogel. However, the mechanical strength of sodium alginate

is relatively poor, so we enhanced the mechanical strength of the microspheres by crosslinking polyacrylic acid (PAA) and sodium alginate (SA) with Ca^{2+}. The addition of PAA facilitated crosslinking with both SA and Ca^{2+}, introducing additional hydrogen bonds and ionic interactions between PAA–PAA, PAA–Ca^{2+}, and PAA–SA, thereby forming a double-cross-linked network composed of PAA, SA, and Ca^{2+}. Additionally, during the preparation of the cyclic adsorption simulated brine solution, we maintained the pH around 6.8. Under these neutral conditions, sodium alginate was less prone to dissolution.[48–50] Due to the affordability and rapid sphere formation of sodium alginate, granulation can be extended to a large scale.

We characterized the morphology of the LMO@SiO$_2$/SA beads using SEM, as shown in Fig. 3b–d. Before freeze-drying, the material is spherical, as depicted in the right image of Fig. 3a, with a smooth surface. After freeze-drying, the overall appearance remains, but the surface becomes relatively rough. The cross-section of the material, shown in Fig. 3c, reveals a loose interior with a dense shell, which further protects the material from dissolution. Fig. 3d shows an enlarged view from the red circle in Fig. 3c, where the distribution of the LMO@-SiO$_2$ powder (indicated by red arrows) is clearly visible. High-magnified SEM and corresponding EDS analysis on this powder are shown in Fig. 3e–g. The figures clearly display the presence of Mn and Si elements, indicating that LMO@SiO$_2$/SA beads contain structures of SiO$_2$, LMO, and the sodium alginate molecular framework, with uniform distribution throughout the composite beads.

Surface area analyses of sodium alginate millimeter beads of LMO@SiO$_2$/SA and HMO@SiO$_2$/SA were conducted using a BET analyzer, as shown in Fig. 4. Before acid washing, the LMO beads appeared black, with a surface area measured by BET of 54.58 m^2 g^{-1} and a pore volume of 9.25 cm^3 g^{-1}, indicating that it functions as a macroporous adsorbent material. The acid wash resulted in the partial dissolution of Mn^{3+}/Mn^{4+} to Mn, changing the bead's color from black LMO to brownish-red HMO, as shown in the inset of Fig. 4. BET measurements showed a slight decrease in the surface area and pore volume of the HMO beads to 46.56 m^2 g^{-1} and 8.87 cm^3 g^{-1}, respectively, confirming that the overall structure remained intact after acid washing.[51]

To evaluate the industrial potential of HMO@SiO$_2$/SA beads for lithium extraction, we established a continuous flow extraction system as depicted in Fig. 5a, with the actual setup shown in Fig. 5b. We simulated a brine solution resembling that of Da Qaidam Salt Lake in Qinghai Province for cyclic testing (Fig. 5c), the specific ion concentrations are given in Table 1. Due to the high concentration of Mg^{2+} in the simulated brine, which could interfere with subsequent ICP analyses, we diluted the solution ten-fold for the adsorption experiments.

The adsorption and desorption results of Li$^+$ from the simulated brine are presented in Fig. 5d. In the initial five cycles, HMO@SiO$_2$/SA beads exhibited an impressive adsorption capacity of 17.6 mg g^{-1} for Li$^+$, with a Mn^{2+} dissolution ratio of 5.2%. However, over the course of 1–25 cycles, the
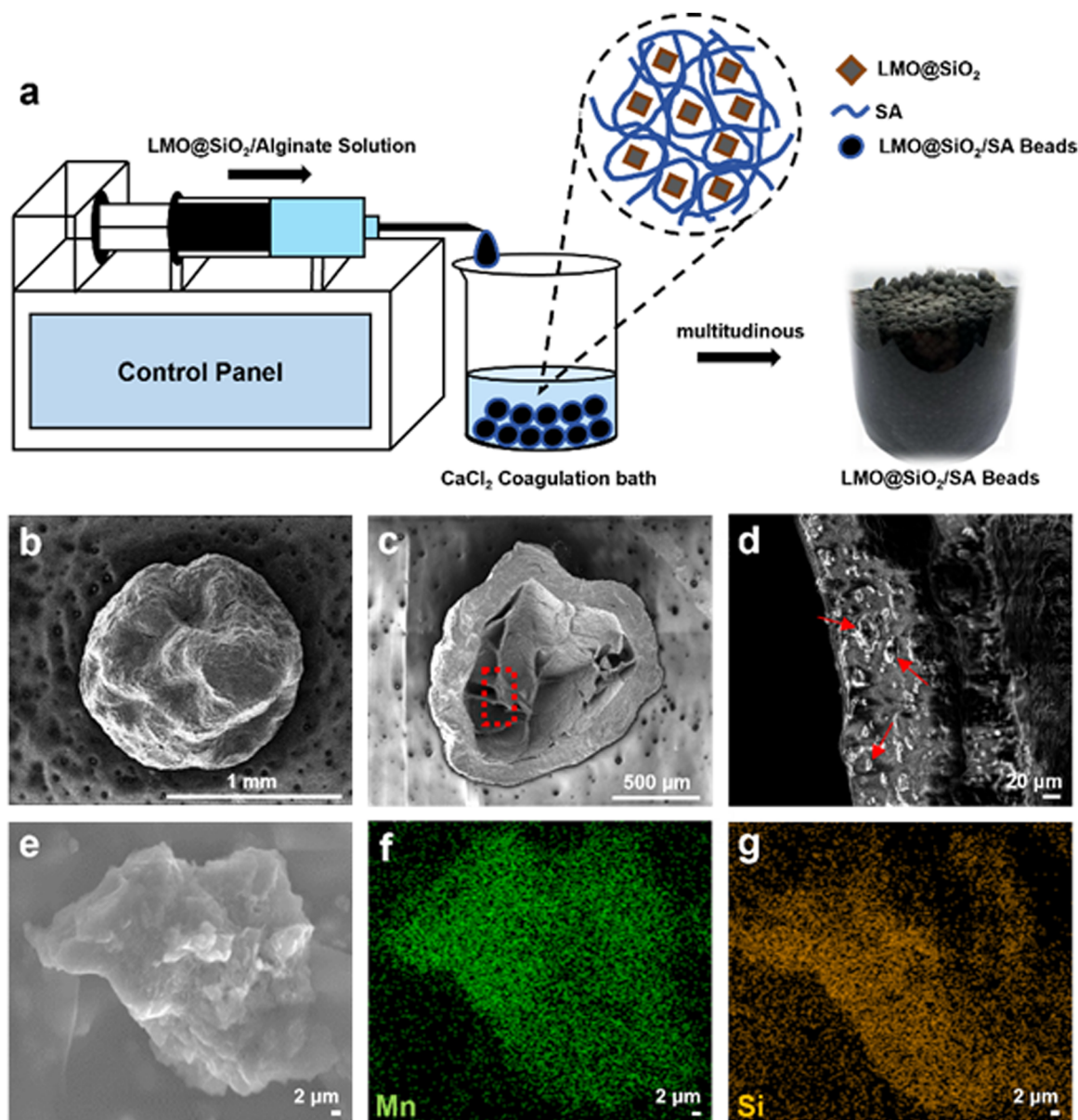
Fig. 3 (a) Schematic of granulation of LMO@SiO$_2$ and actual images of LMO@SiO$_2$/SA beads. (b)–(d) SEM characterization of whole, cross-sectional, and internal venation of LMO@SiO$_2$/SA beads. (e)–(g) High magnified SEM image and the corresponding EDS characterization of Mn and O elements of the embedded LMO@SiO$_2$ powder.

adsorption capacity and the Mn^{2+} dissolution ratio gradually decreased to 7.30 mg g^{-1} and 2.40%, respectively. This decline is likely attributable to the structural damage of the spinel caused by repeated acid washes of the internal HMO. From cycles 30 to 50, the adsorption capacity for Li$^+$ stabilized at approximately 6.22 mg g^{-1}, with an average Mn^{2+} loss ratio of 1.26%. These findings demonstrate that HMO@SiO$_2$/SA beads can effectively extract Li$^+$ from simulated salt lake brine, exhibiting robust stability and lithium extraction capabilities over 50 adsorption–desorption cycles.

And the stability trend observed after 30 cycles in Fig. 5d may be attributed to a combination of surface passivation, manganese dissolution equilibrium, and the formation of stable Li$^+$ transport channels. During the initial cycling stage,

the material undergoes a gradual surface passivation process. A small amount of surface and near-surface manganese ions may dissolve until reaching a dynamic equilibrium. Concurrently, the SiO$_2$ coating layer likely forms a more compact and stable surface structure in the acidic environment, providing continuous protection against further manganese dissolution and structural degradation. Moreover, the repeated insertion and extraction of lithium ions may create stable transport pathways within the material, which reach a relatively fixed state after approximately 30 cycles. This optimization of the internal structure facilitates efficient and stable lithium-ion transport in subsequent cycles. The synergistic effect of these processes results in the observed stability trend post 30 cycles.
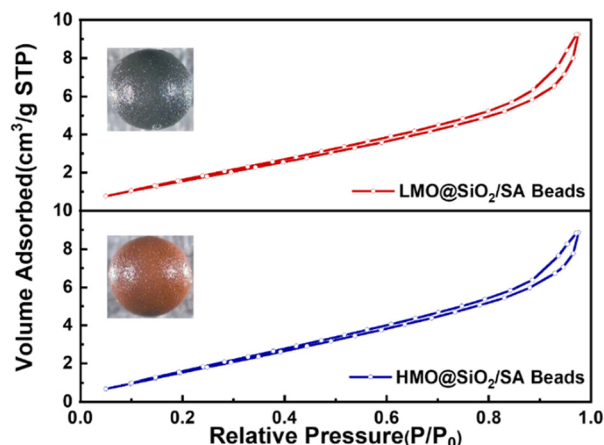
Fig. 4 BET analysis of the adsorption pore volume for LMO@SiO₂/SA beads and HMO@SiO₂/SA beads. Insets are the corresponding single beads before (LMO) and after (HMO) acid treatment.

Conclusions

Our research represents a significant advancement in the field of direct lithium extraction from brine, addressing the growing

Table 1 The main composition of simulated brine

Composition	Li	Na	K	Ca	Mg
Concentration (mg L⁻¹)	330.6	11 882.5	11 737.5	9613.3	18 825

demand for lithium in electric vehicle batteries. By utilizing sodium silicate as the silicon source, we successfully synthesized LMO@SiO₂ composites, yielding a powdered lithium-ion sieve with enhanced structural stability. Notably, in a highly acidic environment (pH = 0.5), the manganese dissolution ratio for LMO@SiO₂ was significantly reduced to 9.33%, compared to 18.02% for uncoated LMO, showing the protective effectiveness of the SiO₂ coating. To simulate real-world industrial applications of this lithium-ion adsorbent in direct lithium extraction from brine, we encapsulated LMO@SiO₂ in sodium alginate beads (LMO@SiO₂/SA beads). The results demonstrate that, in a multi-ion environment with a high Mg/Li ratio, these beads initially exhibited a high adsorption capacity of 17.6 mg g⁻¹, which stabilized at 6.22 mg g⁻¹ after 50 cycles, while maintaining a low average manganese dissolution ratio of 1.26% per cycle. These findings highlight the potential of LMO@SiO₂/SA beads as a promising material for efficient and
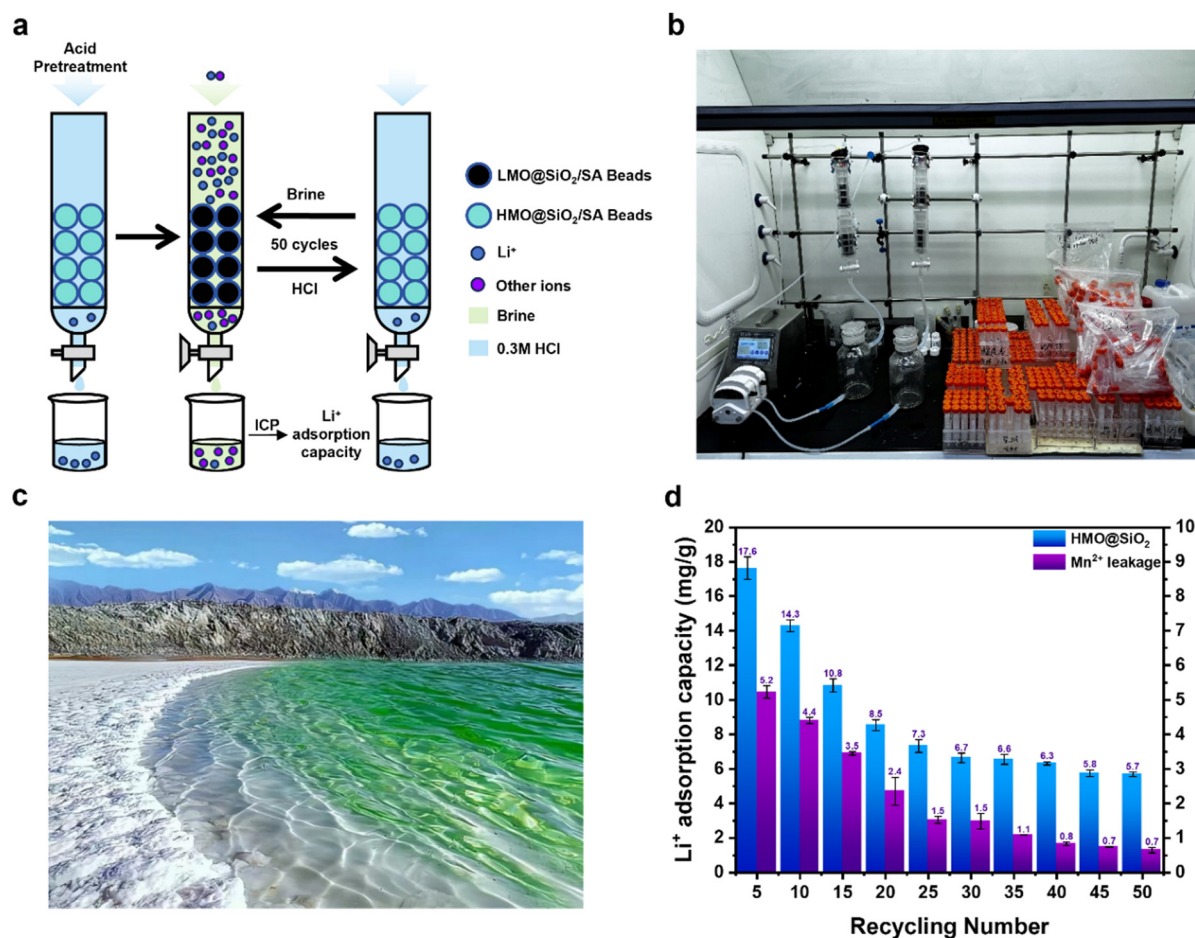

Fig. 5 (a) and (b) Schematic and actual images of the continuous flow adsorption–desorption cycle system. (c) Photograph of Da Qaidam Salt Lake in Qinghai Province. (d) ICP analysis of the Li⁺ adsorption capacity and Mn²⁺ dissolution ratio over 50 cycles.

© 2025 The Author(s). Published by the Royal Society of Chemistry

sustainable lithium extraction from brine, contributing to the development of advanced energy storage solutions.

Author contributions

Jialun Su: investigation, data curation, formal analysis, software, validation, visualization, and writing – original manuscript draft; Qiyue Fan: investigation, data curation, formal analysis, software, validation, visualization, and writing – original manuscript draft; Xiangting Hu: formal analysis, methodology, and software; Yue Sun: formal analysis, methodology, and software; Jie Lin: methodology and software; Jiayue Xu: methodology and software; Bingcai Pan: validation; Zhenda Lu: funding acquisition, conceptualization, methodology, project administration, supervision, and writing – review and editing.

Data availability

The authors confirm that the data supporting the findings of this study are available within the article.

Conflicts of interest

There are no conflicts to declare.

Acknowledgements

Notes and references

1 H. Li, J. Pan, Y. Ping, J. Su, M. Fang, T. Chen, B. Pan and Z. Lu, *Nano Lett.*, 2023, **23**, 10458–10465.
2 B. Dunn, H. Kamath and J.-M. Tarascon, *Science*, 2011, **334**, 928–935.
3 S. E. Kesler, P. W. Gruber, P. A. Medina, G. A. Keoleian, M. P. Everson and T. J. Wallington, *Ore Geol. Rev.*, 2012, **48**, 55–69.
4 A. Alessia, B. Alessandro, V.-G. Maria, V.-A. Carlos and B. Francesca, *J. Cleaner Prod.*, 2021, **300**, 126954.
5 J.-M. Tarascon and M. Armand, *Nature*, 2010, **414**, 359–367.
6 L. V. Garcia, Y.-C. Ho, M. M. Myo Thant, D. S. Han and J. W. Lim, *Processes*, 2023, **11**, 418–441.
7 M. M. Thackeray, C. Wolverton and E. D. Isaacs, *Energy Environ. Sci.*, 2012, **5**, 7854–7863.
8 M. Zhang, H. Tian, H. Wei, P. Tian, C. Yu and Z. Zhao, *Rare Met. Cem. Carbides*, 2018, **46**, 11–19.
9 M. L. Vera, W. R. Torres, C. I. Galli, A. Chagnes and V. Flexer, *Nat. Rev. Earth Environ.*, 2023, **4**, 149–165.
10 Y. Zeng, W. Li, Z. Wan, S. Qin, Q. Huang, W. Cai, Q. Wang, M. Yao and Y. Zhang, *Adv. Funct. Mater.*, 2024, 2400416.
11 J. Li, S. Zhu and Z. Li, *Sci. Sin.: Chim.*, 2017, **47**, 1273–1283.
12 R. Xie, Z. Zhao, X. Tong, X. Xie, Q. Song and P. Fan, *Particuology*, 2024, **87**, 46–53.
13 T. Kundu, S. S. Rath, S. K. Das, P. K. Parhi and S. I. Angadi, *Powder Technol.*, 2023, **415**, 118142.
14 M. Anik Hasan, R. Hossain and V. Sahajwalla, *Process Saf. Environ. Prot.*, 2023, **178**, 976–994.
15 Y. Hu, H. Su, Z. Zhu, T. Qi and Q. Pang, *Environ. Chem. Lett.*, 2024, **22**, 105–120.
16 M. Zhao, C. Zhao, Y. Zhang, J. Luan, G. Pan, C. Han, H. Peng, H. Yu, G. Zhao, G. Tang, Y. Li, X. Zhang and Y. Liu, *J. Environ. Chem. Eng.*, 2023, **11**, 110859.
17 H. Wang, J. Cui, M. Li, Y. Guo, T. Deng and X. Yu, *Chem. Eng. J.*, 2020, **389**, 124410.
18 J. Yang, Y. Wang, M. Zhang, P. Wang, X. He, H. Zhou and P. He, *Angew. Chem., Int. Ed.*, 2024, e202411957.
19 R. Zhu, *Environ. Chem. Lett.*, 2023, **21**, 1611–1626.
20 A. H. Hamzaoui, A. Mnif, H. Hammi and R. Rokbani, *Desalination*, 2003, **158**, 221–224.
21 M. Pasta, A. Battistel and F. La Mantia, *Energy Environ. Sci.*, 2012, **5**, 9487–9491.
22 C. P. Lawagon, G. M. Nisola, R. A. I. Cuevas, H. Kim, S.-P. Lee and W.-J. Chung, *Chem. Eng. J.*, 2018, **348**, 1000–1011.
23 J. M. Tarascon and D. Guyomard, *J. Electrochem. Soc.*, 1991, **138**, 2864–2868.
24 S. Kim, J. Lee, J. S. Kang, K. Jo, S. Kim, Y.-E. Sung and J. Yoon, *Chemosphere*, 2015, **125**, 50–56.
25 J. Lee, S.-H. Yu, C. Kim, Y.-E. Sung and J. Yoon, *Phys. Chem. Chem. Phys.*, 2013, **15**, 7690–7695.
26 J. Wang and G. M. Koenig, *Chem. – Eur. J.*, 2024, **30**, 2776–2798.
27 A. Battistel, M. S. Palagonia, D. Brogioli, F. La Mantia and R. Trócoli, *Adv. Mater.*, 2020, **32**, 1905440–1905462.
28 Y. Chen, F. Zhang, Y. Wang, C. Yang, J. Yang and J. Li, *Microporous Mesoporous Mater.*, 2018, **258**, 170–177.
29 L. Zhang, D. Zhou, G. He, Q. Yao, F. Wang and J. Zhou, *Mater. Lett.*, 2015, **145**, 351–354.
30 R. Chitrakar, Y. Makita, K. Ooi and A. Sonoda, *Dalton Trans.*, 2014, **43**, 8933–8939.
31 R. Chitrakar, H. Kanoh, Y. Miyai and K. Ooi, *Ind. Eng. Chem. Res.*, 2001, **40**, 2054–2058.
32 K. Ooi, Y. Miyai and S. Katoh, *Sep. Sci. Technol.*, 1986, **21**, 755–766.
33 X. Luo, K. Zhang, J. Luo, S. Luo and J. Crittenden, *Environ. Sci. Technol.*, 2016, **50**, 13002–13012.
34 S. Zhang, X. Wei, X. Cao, M. Peng, M. Wang, L. Jiang and J. Jin, *Nat. Commun.*, 2024, **15**, 238–246.
35 R. Trócoli, C. Erinmwingbovo and F. La Mantia, *Chem. Electro. Chem.*, 2017, **4**, 143–149.
36 M. J. Park, G. M. Nisola, A. B. Beltran, R. E. C. Torrejos, J. G. Seo, S.-P. Lee, H. Kim and W.-J. Chung, *Chem. Eng. J.*, 2014, **254**, 73–81.

37 H. Li, T. Chen, J. Jiang, G. Gao, C. Wang and Z. Lu, *Chem. Eng. J.*, 2023, **451**, 138662.

38 H. Li, T. Chen, W. Wang, G. Gao and Z. Lu, *Chem. Nano. Mater.*, 2022, **8**, 324–330.

39 B. Ammundsen, D. J. Jones, J. Rozière, H. Berg, R. Tellgren and J. O. Thomas, *Chem. Mater.*, 1998, **10**, 1680–1687.

40 A. Gao, Z. Sun, S. Li, X. Hou, H. Li, Q. Wu and X. Xi, *Dalton Trans.*, 2018, **47**, 3864–3871.

41 J. Xiao, X. Nie, S. Sun, X. Song, P. Li and J. Yu, *Adv. Powder Technol.*, 2015, **26**, 589–594.

42 Z. Xie, H. Eikhuemelo, J. Zhao, C. Cain, W. Xu and Y. Wang, *J. Electrochem. Soc.*, 2015, **162**, 1523–1529.

43 W. Xiao, C. Xin, S. Li, J. Jie, Y. Gu, J. Zheng and F. Pan, *J. Mater. Chem. A*, 2018, **6**, 9893–9898.

44 H.-J. Hong, T. Ryu, I.-S. Park, M. Kim, J. Shin, B.-G. Kim and K.-S. Chung, *Chem. Eng. J.*, 2018, **337**, 455–461.

45 Z.-Y. Ji, M.-Y. Zhao, J.-S. Yuan, J. Wang, J.-Q. Zhou, H.-B. Yin and B.-Y. Sun, *Solvent Extr. Ion Exch.*, 2016, **34**, 549–557.

46 J. C. Hunter, *J. Solid State Chem.*, 1981, **39**, 142–147.

47 B. Ammundsen, D. J. Jones, J. Roziere and G. R. Burns, *Chem. Mater.*, 1995, **7**, 2151–2160.

48 R. Abka-khajouei, L. Tounsi, N. Shahabi, A. K. Patel, S. Abdelkafi and P. Michaud, *Mar. Drugs*, 2022, **20**, 364–381.

49 S. Kumar and D. Sahoo, *Algal Res.*, 2017, **23**, 233–239.

50 S. Jothisaraswathi, B. Babu and R. Rengasamy, *J. Appl. Phycol.*, 2006, **18**, 161–166.

51 I. P. S. Fernando, W. Lee, E. J. Han and G. Ahn, *Chem. Eng. J.*, 2020, **391**, 123823.